Pergamon

International Journal of Machine Tools & Manufacture 39 (1999) 33–53

INTERNATIONAL JOURNAL OF
MACHINE TOOLS
& MANUFACTURE
DESIGN, RESEARCH AND APPLICATION

A three-dimensional CAD/CAM/CAE integration system of sculpture surface die for hollow cold extrusion

Jinn-Jong Sheu

Department of Mold and Die Engineering, National Kaohsiung Institute of Technology, 415 Chien-Kung Road, Kaohsiung 807, Taiwan, R.O.C.

Received 30 June 1997; in final form 28 January 1998

Abstract

In this paper, a CAD/CAM/CAE integration system for a sculptured surface die for hollow cold extrusion has been developed by using C language for Windows. A sculptured surface model with variable control points is incorporated with a general three-dimensional velocity field to analyze the extrusion process. The profiles of the product and the billet are generated in the CAD module. The fitting points are generated to interpolate the profiles of the product and the billet. The initial guess of control points are created by using the offset of corresponding fitting points in the axial direction. The control points are varied automatically to obtain the optimum die surface by using the upper-bound method and optimization procedure. The CAM module generates the cutter locations by using the optimized die surface model. The gouging areas of the tool path are detected and removed. The calculated cutter locations are verified through the tool path simulation. The NC codes are generated automatically by using the gouging-free cutter locations and then sent directly to a three-axis CNC machine centre to manufacture the EDM electrodes. The extrusion die cavity is made by using an EDM process. Extrusion experiments have verified the proposed CAD/CAM/CAE integration system is successful.

Keywords: CAD/CAM/CAE integration; Upper-bound; Cold extrusion; Sculpture surface

Nomenclature

a,b,c,d,e,h, the optimum parameters of velocity field

p,q

$C(\theta,z)$ $\quad \dfrac{R_m^2}{2} V_m(z) + \dfrac{R_m^{q+1}}{q+1} \dfrac{\partial \Omega(\theta,z)}{\partial \theta}$

$\overrightarrow{B,B'}$ control points of the entrance boundary before and after optimization

0890-6955/99/$—see front matter
PII: S0890-6955(98)00029-7

dA	incremental area on the exit section
$\overrightarrow{E}$	control points of the exit boundary
$F(u)$	Hermite form blending function
$g(\beta)$	$\beta^3 + a\beta^2 + b\beta + c$, shape function of the z-direction velocity
H	the tooth height of a fin-tube
$h_{\max}$	the allowable maximum cusp height
J^*	total extrusion power consumption
L, L/R_b	the die length and the relative die length
m	constant shear friction factor
P	the extrusion pressure required
P^*	composition of the position, u-, v-derivative and twist vectors
P_i	fitting points of a sculpture surface
P_{lb}, P_{lt}, P_{rb}, P_{rt}	fitting points of a surface patch
$\overrightarrow{Q}$, $\overrightarrow{P}$	fitting points of the entrance and the exit boundaries, respectively
$R(u,v)$	sculpture surface model
R, $R(\theta,z)$	the die surface
$R1$	the base circle radius of a fin-tube
R_b, R_m, $R_h(\theta,z)$	the radius of the billet, the mandrel, $hR(\theta,z) + (1-h)R_m$
$V_m(z)$	the average longitudinal velocity
$V_m'(z)$	the derivative of average longitudinal velocity w.r.t. z
V_r, V_z, V_θ	the velocities in the r-, z-, θ-directions
V_{ram}, V_{exit}	the ram speed and the exit velocity
$\dot{W}_i$, $\dot{W}_{fd}$, $\dot{W}_{fm}$	internal power, frictional powers of die surface and mandrel
r, z, θ	the cylindrical coordinate
u, v	normalized parameters of surface model
θ_b, θ_e	lower and upper bound of integration along the θ directions
$\alpha(z)$	$dz^2(z-e)(z-L)^2$
β	$(r - R_m)/[R(\theta,z) - R_m]$
Γ_{exit}	the plane of the exit section
$\bar{\epsilon}_{favg}$	the average total effective strain at the exit section
$\bar{\epsilon}_f = \int_0^t \dot{\bar{\epsilon}}\,dt$	the final strain integrated along a constant stream-line
$\dot{\epsilon}_r$, $\dot{\epsilon}_z$, $\dot{\epsilon}_\theta$	strain rate components
$\dot{\epsilon}_{rz}$, $\dot{\epsilon}_{r\theta}$, $\dot{\epsilon}_{z\theta}$	strain rate components
$\dot{\bar{\epsilon}}$	effective strain rate
$\bar{\sigma}$, $\bar{\sigma}_m$	effective and mean effective flow stress
$\eta\ (\theta, z)$	$R_h^p(\theta,z)$
$\Delta\ (\theta, z)$	$R(\theta,z) - R_m$
$\Omega(\theta, z)$	$\dfrac{-(q+1)}{2(R^{q+1} - R_m^{q+1})} \int_0^\theta \dfrac{\partial(R^2 V_m - R_m^2 V_m)}{\partial z}\,d\theta$

1. Introduction

The traditional design for a non-axisymmetric extrusion is a conical or a flat-face die. As a result, a high extrusion load is required and the material flow is not well controlled. The design of a flat-face die is very experience-dependent and time consuming. A CAD/CAM/CAE integration system has been developed to shorten the lead times of die design and manufacturing.

There are many die design and material flow prediction methods proposed by researchers. The upper bound method is a simple and applicable approach to analyze the material flow of the extrusion process. Kiuchi et al. [1–4] have proposed a linearly converging die with the assumption of uniform axial flow to analyze many non-axisymmetric section extrusion. Nagpal et al. [5] have used a polynomial function to design a streamlined die for the extrusion of 'T' sections. Hoshino and Gunasekera [6,7] have proposed a velocity filed for polygon shape extrusion with the linearly converging and the cubic streamlined dies. Yang and Lange [8] proposed a more general velocity field with the assumption of uniform axial velocity. Yang et al. [9–11] has proposed a general three-dimensional velocity field for the die surface that can be expressed by an analytical function. Yang et al. [9] used a Fourier series expansion method to describe the die surface that can't be expressed analytically. Yang et al. [12] had proposed a general three-dimensional velocity filed to predict the hollow extrusion process with an analytical expression of die surface. The linearly converging dies had the abrupt velocity discontinuity and additional shear consumption required. The application of die surface with analytical function description has its limitation. The cubic streamlined die neglects the effect of die geometry on the material flow in the circumference direction. The Fourier series expansion method is flexible but unnatural to present a die surface for cutting path generation. Sheu et al. [13] had proposed a surface model with tension parameter and adopted a general three-dimensional velocity field to predict the solid extrusion process. In this paper, a sculptured surface model with variable control points is proposed to design a die surface for hollow extrusion. It is convenient and flexible to describe the shape of product and the geometry of die. The NC tool path calculation of a surface model is also well-developed. The optimum die surface data is directly used to plan the tool path and calculate the cutter locations in the CAM module. The surface model enables the smooth CAD/CAE/CAM integration of the proposed system.

There are many approaches and considerations to generate the cutter locations and the NC codes for the manufacturing of a three-dimensional surface. Faux and Pratt [14] proposed the offset surface method to calculate the cutter locations. Broomhead [15] considered the tolerances in the forward and the side directions and calculated the step length in the cutting direction and in the neighbouring tool path by using an iteration method. Loney and Ozsoy [16] applied the chord error method to determine the increment of the cutter centre along the cutting path. The cutting step of the neighbouring paths is determined by considering the scallop height. The interference paths are removed to generate the gouging-free cutter locations (Choi et al. [17]).

In this paper, the NC tool path is planned on the parametric-space of the sculptured surface. The parameter increment is set to 0.05 in the forward direction and then filtered by using the chord deviation method. The cutter locations are calculated by using the normal vector of the optimized die surface. The gouging areas of the tool path are checked and removed by using the curvature examination and the self-loop detection. The traces of cutter locations are displayed graphically to simulate the cutting process. The cutting conditions, such as the dimension of cutter

and the feed rate, and the cutter locations are used by the CAM module to generate the NC codes automatically.

2. The structure of the integration system

The block diagram of the proposed integration system is shown in Fig. 1. A general graphic user interface (GUI) has been established to communicate with users and show the results of the CAD/CAE/CAM modules by using C language. The product and the billet profiles are drawn by using line and arc entities. The fitting points and the correspondent control points are generated automatically in the CAD module to interpolate the profiles and to control the *v*-derivatives of the surface model. The surface model is incorporated with the velocity field, the CAE module uses the upper-bound method and the optimization process to optimize the die surface. The optimum die surface is displayed with the shading algorithm or the hidden line removal scheme.

The material property and the lubrication condition are input in the CAE module. The power law is used to present the flow stress of the material. The constant shear friction factor, *m*, is used to consider the friction conditions. The die length can be fixed or varied during the die surface optimization procedures. An optimization die surface is automatically designed in the CAE module by using the upper-bound analysis to minimize the extrusion load. The cutter geometry and the cutting parameters, such as tolerance and cutting speed, are input in the CAM module. The optimum die surface data is directly used by the CAM module to plan the cutting path and to calculate the cutter locations. The gauging of cutter is detected and removed by using the interference checking and removal procedure. The NC program is generated automatically by using the gouging-free cutter locations and the cutting parameters. The NC codes are sent to a three-axis CNC machine centre to manufacture the electrodes of EDM.

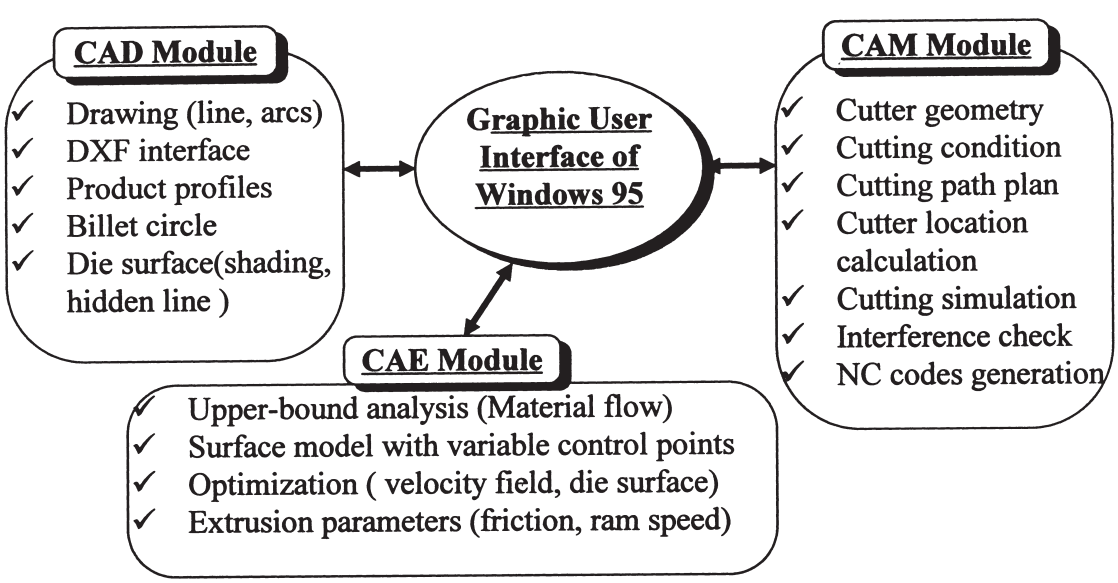

Fig. 1. The schematic diagram of the proposed CAD/CAM/CAE integration system.

3. The surface model with variable control points

A sculptured surface model with the variable control points is proposed to describe the die geometry. The schematic diagram of a sculpture surface and the fitting points is shown in Fig. 2. The surface model is composed from the fitting points and the patches. The surface is represented by using u-direction and v-direction surface curves in the (u,v) parameter space. The mathematical representation of a sculpture surface is as follows:

$$R(u,v) = F(u)P^*F^T(v) \tag{1a}$$

where $F(u)$ is the Hermite form blending function, $F(u)$ is given as

$$F(u) = [1\ u\ u^2\ u^3]\begin{bmatrix} 1 & 0 & 0 & 0 \\ 0 & 0 & 1 & 0 \\ -3 & 3 & -2 & -1 \\ 2 & -2 & 1 & 1 \end{bmatrix} \tag{1b}$$

$$P^* = \begin{bmatrix} [\text{position vectors}] & [v-\text{derivative vectors}] \\ [u-\text{derivative vectors}] & [\text{twisting vectors}] \end{bmatrix} \tag{1c}$$

In Eq. (1c), the twisting vectors of the fitting points are set to zero to obtain a smooth die surface. The vectors of the u-derivative and the v-derivative are obtained by using the slope continuity requirement of the neighbouring patches and the boundary conditions. The u-direction means the circumference direction of the die surface. The u-derivatives of the fitting points are obtained by using the spline fitting of the product and billet profiles. The v-direction means the axial longitudinal direction of the die surface. The v-derivative of the fitting points are controlled

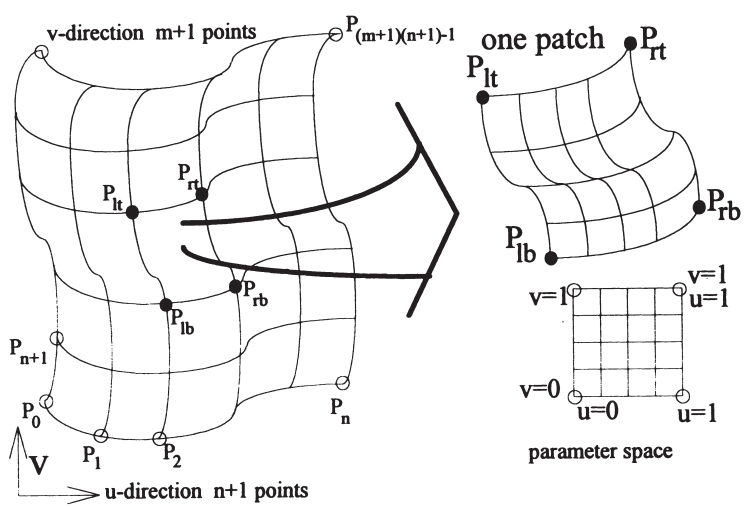

Fig. 2. The schematic diagram of the sculptured surface and fitting points.

by varying the positions of the correspondent control points. The optimum die surface with lower energy consumption is obtained by changing the positions of control points. Fig. 3 shows the fitting points $\vec{Q}$, $\vec{P}$ and the correspondent control points $\vec{B}$, $\vec{E}$ on a *v*-direction curve. The *x*,*y*-coordinates of the control points are same as the correspondent fitting points, but the *z*-coordinate is different. The variation of the *z*-coordinate of control points $\vec{B}$, $\vec{E}$ changes the correspondent *v*-derivative of the fitting points $\vec{Q}$, $\vec{P}$ and as a result, the die surface is changed. The original *v*-curve with the control point $\vec{B}$ is shown by a solid line and the varied *v*-curve with the control point $\vec{B}'$ is shown by a dashed line in Fig. 3. The *z*-coordinate of the control points $\vec{B}$, $\vec{E}$ are divided by the die length *L* to obtain the normalized parameters for surface optimization. The final position of the control points are determined by using an optimization process and the upper bound analysis.

The hidden line removing and the rendering schemes are used to display the optimum die surface more comprehensively. The well-known *z*-buffer scheme is adopted to remove the hidden lines. The well-developed Gourand shading algorithm is adopted to render the surface and eliminate the intensity discontinuities caused by the constant shading.

4. The upper bound analysis

The upper bound analysis method is adopted to simulate the hollow cold extrusion process. The surface model is incorporated with a kinematically admissible velocity field [12] to predict the material flow. The velocity field should satisfy the boundary conditions and the volume constancy of material during the extrusion process. The following assumptions are made to derive the velocity field:

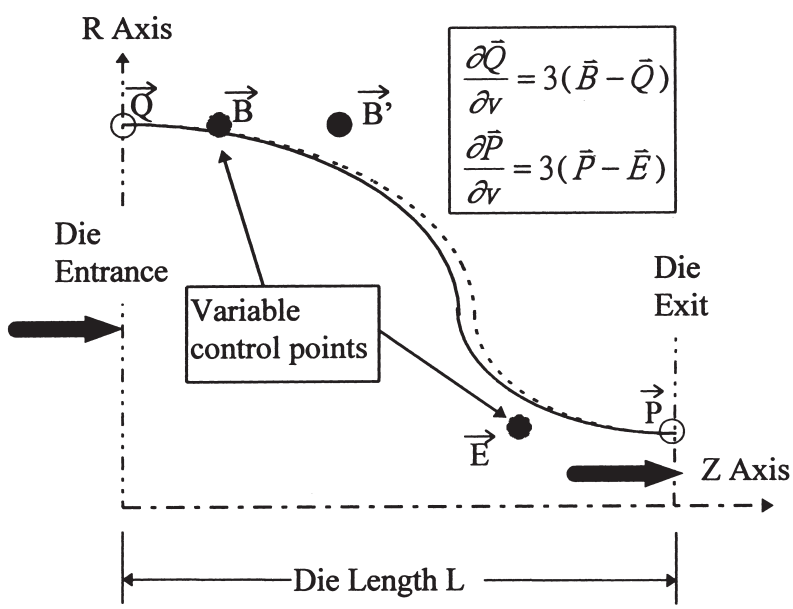

Fig. 3. The variable control points of a surface curve for surface optimization.

1. The cross-section of the material in the die entrance and the die exit are all planes.
2. The material is incompressible and obey the von Mises yield criterion.
3. The material deformation follows the rigid-plastic model.

By referring to the notations in Fig. 4 and using the above mentioned assumptions, the velocity field is obtained as follows:

(a) the non-uniform axial velocity (longitudinal velocity) is assumed to be

$$V_z(r,\theta,z) = V_m(z) + a(z)R_h^p(\theta,z)g(\beta) \tag{2a}$$

$$V_m(z) = \frac{v_{ram}\int_0^{2\pi} R^2(\theta,0)\mathrm{d}\theta}{\int_0^{2\pi} R^2(\theta,z)\mathrm{d}\theta} \tag{2b}$$

$$\alpha(z) = \mathrm{d}z^2(z-e)(z-L)^2 \tag{2c}$$

$$\beta = (r - R_m)/[R(\theta,z) - R_m] \tag{2d}$$

$$R_h(\theta,z) = hR(\theta,z) + (1-h)R_m \tag{2e}$$

$$g(\beta) = \beta^3 + a\beta^2 + b\beta + c \tag{2f}$$

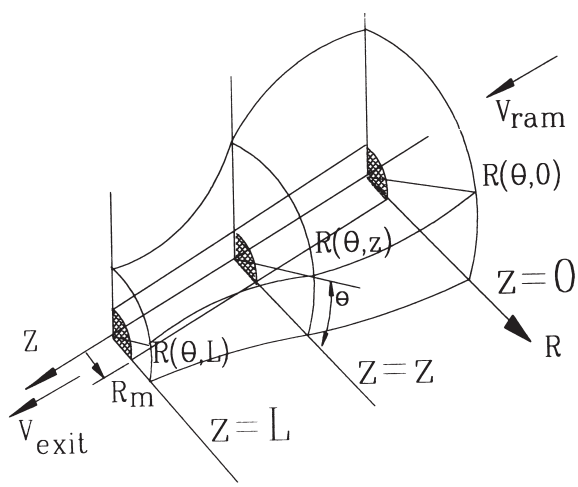

Fig. 4. The notation and boundaries of the kinematically admissible velocity field.

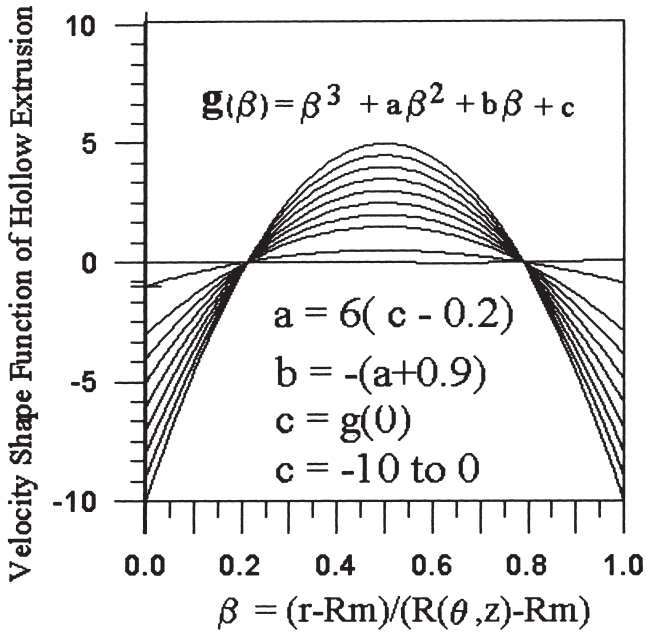

Fig. 5. The shape function of *z*-direction velocity for hollow extrusion.

where $R(\theta,z)$ is the die surface, R_m is the radius of the mandrel, $V_m(z)$ is the average longitudinal velocity, V_{ram} is the ram speed, *a*, *b*, *c*, *d*, *e*, *h*, *p* are the optimum parameters of the velocity field, $g(\beta)$ is the shape function of V_z. Fig. 5 shows the shape function of axial velocity for hollow extrusion. By applying the incompressible conditions, the parameters *a*, *b* and *c* are not independent, the relations are given as follows:

$$3/20 + a/6 + b/6 = 0 \tag{3a}$$

$$1/4 + a/3 + b/2 + c = 0 \tag{3b}$$

(b) the angular velocity is assumed to be

$$V_\theta(r,\theta,z) = r^q \Omega(\theta,z) \tag{4}$$

(c) the radial velocity is derived from the incompressible assumption and is given by

$$V_r(r,\theta,z) = -\frac{r}{2} V_m' - \frac{\Delta}{r}(\alpha'\eta + \alpha\eta')\left[\Delta\left(\frac{\beta^5}{5} + \frac{a\beta^4}{4} + \frac{b\beta^3}{3} + \frac{c\beta^2}{2}\right) + R_m\left(\frac{\beta^4}{4} + \frac{a\beta^3}{3} + \frac{b\beta^2}{2} + c\beta\right)\right] + \frac{\alpha\eta}{r}\left(\frac{3\beta^4}{4} + \frac{2a\beta^3}{3} + \frac{b\beta^2}{2}\right)R'(\theta,z)R_m \tag{5a}$$

$$+\frac{\alpha\eta\Delta}{r}\left(\frac{3\beta^5}{5}+\frac{2a\beta^4}{4}+\frac{b\beta^3}{3}\right)R'(\theta,z)$$
$$-\frac{r^q}{q+1}\frac{\partial\Omega(\theta,z)}{\partial\theta}+\frac{C(\theta,z)}{r}$$

$$\Delta(\theta,z)=R(\theta,z)-R_{\mathrm{m}} \tag{5b}$$

$$\eta(\theta,z)=R_h^p(\theta,z)$$

$$C(\theta,z)=\frac{R_{\mathrm{m}}^2}{2}V_{\mathrm{m}}(z)+\frac{R_{\mathrm{m}}^{q+1}}{q+1}\frac{\partial\Omega(\theta,z)}{\partial\theta} \tag{5c}$$

$$\Omega(\theta,z)=\frac{-(q+1)}{2(R^{q+1}-R_{\mathrm{m}}^{q+1})}\int_0^{\theta}\frac{\partial(R^2V_{\mathrm{m}}-R_{\mathrm{m}}^2V_{\mathrm{m}})}{\partial z}\,\mathrm{d}\theta \tag{5d}$$

where ($'$) means first derivative with respect to z. In order to obtain a smooth die surface, the v-direction tangent vectors in the die entrance and the exit boundaries should be zero at the die entrance and die exit, as a result, the fitting points and the correspondent control points should have the same (x,y) coordinates. The strain rate field is obtained by the derivation of the above mentioned velocity field and is given as follows:

$$\dot{\epsilon}_r=\partial V_r/\partial r$$
$$\dot{\epsilon}_z=\partial V_z/\partial z \tag{6a}$$
$$\dot{\epsilon}_\theta=V_r/r$$

$$\dot{\epsilon}_{rz}=\frac{1}{2}\left[\partial V_z/\partial r+\partial V_r/\partial z\right]$$
$$\dot{\epsilon}_r\theta=\frac{1}{2}\left[\frac{1}{r}\,\partial V_r/\partial\theta+\partial V_\theta/\partial r-V_\theta/r\right] \tag{6b}$$
$$\dot{\epsilon}_z\theta=\frac{1}{2}\left[\frac{1}{r}\,\partial V_z/\partial\theta+\partial V_\theta/\partial z\right]$$

$$\bar{\dot{\epsilon}}=\left[\frac{2}{3}\left(\dot{\epsilon}_r^2+\dot{\epsilon}_\theta^2+\dot{\epsilon}_z^2+\dot{\epsilon}_{r\theta}^2+\dot{\epsilon}_{\theta z}^2+\dot{\epsilon}_{zr}^2\right)\right]^{1/2} \tag{6c}$$

The velocity field is continuous at the entrance and the exit sections and no shear power consumption vanishes here. The total extrusion power required consists of the internal power and the frictional powers and is given by

$$J^* = \dot{W}_{\mathrm{i}} + \dot{W}_{\mathrm{fd}} + \dot{W}_{\mathrm{fm}} \tag{7}$$

The internal power consumption of deformation is given by

$$\dot{W}_{\mathrm{i}} = \int_v \bar{\sigma}\,\dot{\bar{\epsilon}}\,\mathrm{d}v = \sqrt{\frac{2}{3}}\bar{\sigma}_{\mathrm{m}} \int_0^L \int_0^{2\pi} \int_{R_{\mathrm{m}}}^{R(\theta,z)} (\dot{\epsilon}_{\mathrm{ij}}\dot{\epsilon}_{\mathrm{ij}})^{1/2} r\,\mathrm{d}r\,\mathrm{d}\theta\,\mathrm{d}z \tag{8}$$

where L is the die length, $\dot{\epsilon}ij$ is the strain rate components, and $\bar{\sigma}_{\mathrm{m}}$ is the mean effective stress for work-hardening material and is approximated by the following equation:

$$\bar{\sigma}_{\mathrm{m}} = \int_0^{\bar{\epsilon}_{\mathrm{favg}}} \bar{\sigma}\,\mathrm{d}\bar{\epsilon} / \bar{\epsilon}_{\mathrm{favg}} \tag{9}$$

where $\bar{\epsilon}_{\mathrm{favg}}$ is the average total effective strain at the exit section Γ_{exit} and is obtained by

$$\bar{\epsilon}_{\mathrm{favg}} = \int_{\Gamma_{\mathrm{exit}}} \bar{\epsilon}_{\mathrm{f}}\,\mathrm{d}A \Big/ \int_{\Gamma_{\mathrm{exit}}} \mathrm{d}A \tag{10}$$

where $\bar{\epsilon}_{\mathrm{f}} = \int_0^t \dot{\bar{\epsilon}}\,\mathrm{d}t$ is the final strain by integrating the effective strain rate along a constant streamline. The frictional power dissipated along the die surface is given by

$$W_{\mathrm{fd}} = \frac{2\pi m}{\sqrt{3}}\,\sigma_{\mathrm{m}} \int_0^L [V_r^2 + V_z^2]_{r=R}^{1/2} R \left[1 + \left(\frac{\partial R}{R\partial\theta}\right)^2 + \left(\frac{\partial R}{\partial z}\right)^2\right]^{1/2} \mathrm{d}z\,\mathrm{d}\theta \tag{11}$$

where m is the constant shear friction factor between the billet and the die surfaces. The frictional power dissipated along the mandrel surface is given by

$$\dot{W}_{\mathrm{fm}} = \frac{2\pi m}{\sqrt{3}}\,\bar{\sigma}_{\mathrm{m}} R_{\mathrm{m}} L [V_r^2 + V_z^2]_{r=R_{\mathrm{m}}}^{1/2} \tag{12}$$

where m is the friction factor between the billet and the mandrel surfaces. The parameters of the velocity field and the die surface are determined by using the optimization method to minimize the extrusion pressure required. Here, the variable metric optimization scheme [18] is adopted to obtain the optimization die surface. The extrusion pressure is obtained by

$$P = (\dot{W}_{\mathrm{i}} + \dot{W}_{\mathrm{fd}} + \dot{W}_{\mathrm{fm}}) / [\pi(R_{\mathrm{b}}^2 - R_{\mathrm{m}}^2) V_0] \tag{13}$$

5. The NC tool path planning and the cutter location calculation

The tool paths are calculated in the circumference direction clockwise. The roughing tool path is planned on the constant Z planes. The flat-end mill is used for roughing in order to obtain a high material removal rate. The tool paths of finishing are generated along the stream lines of constant v parameter. The ball-end mill is adopted in the finishing operation to follow the surface model smoothly. The cutter locations of the finish cutting are calculated by using the surface normal offset. The tolerance of chord error is used to determine the cutting step in the circumferential direction. The algorithm is as follows:

1. Generate the testing points: the interpolation points are generated with a small u interval (0.05) between two fitting points.
2. Calculate the deviation of the interpolation points: find the chord deviation of the interpolation points with respect to the line entity construct by the start and the marching points.
3. Filter the interpolation points: if the chord deviation is smaller than the tolerance, the interpolation point next to the marching point is set to a new marching point.
4. Repeat (2) and (3): iterate until the chord deviation is larger than the tolerance, the point prior to the marching point is the stop point of this step and start point of next step.

The cutting step in the z-direction is determined by checking the approximation cusp, i.e. the cutting step must be smaller than $2\sqrt{h_{\max}(2R_c - h_{\max})}$, where $h_{\max}$ is the allowable cusp height. The interference areas of the cutter location are eliminated by checking the principal curvature and the minimum curvature [17].

6. Experimentation

Cylinder upsetting tests and the ring compression tests were carried out to determine the flow stress of the aluminum 1100 F and the constant shear friction factor m between the die-material interface. The flow stress of aluminum 1100 F was found to be $162.329\bar{\epsilon}^{0.41381}$ MPa and the friction factor 0.18 from the compression tests. The extrusion experiments were carried out to verify the theoretical results. A Saginomiya 100-ton hydraulic press shown in Fig. 6 with load, speed and displacement control was used for the compression and extrusion tests. The hollow billets for extrusion tests were 30 mm outer diameter, 50 mm high and either 10 mm, 14 mm or 18 mm inner diameter. The diameters of the mandrel were either 10, 14 or 18 mm, respectively. The components of the extrusion die set are shown in Fig. 7 including the container, ram, mandrels, bolster and die cavity.

7. Results and discussion

7.1. Description of the product profiles and the optimum design of die surface

Fig. 8 shows the profiles and the fitting points of a gear spline created by using the CAD functions of the proposed system. The z coordinate of the control points are varied automatically

Fig. 6. The Saginomiya 100-ton hydraulic press for compression and extrusion tests.

to find an optimum die geometry to minimize the required extrusion load. Fig. 9 shows the optimum die surface obtained automatically which has a smooth transition at the die entrance and die exit. The different views and the shading results of the die surface are displayed to help the comprehension of the designers. These two figures have shown the ability of die surface design automation of the proposed system by using the functions of CAD and CAE modules.

7.2. Die manufacturing

The tool path simulation of the cutting operations are shown in Fig. 10(a,b). A flat-end cutter is used for the rough cutting and a ball-end cutter is used for the finish cutting. The spindle speed is 1200 rpm, the feed rate is 100 mm/min, the allowance for finishing is 0.1 mm. The staring point of the cutting is at the top centre of the electrode. The interference of the cutter locations in the finish cutting should be removed. Fig. 11(a) shows the gauging of the tool path occurred

Fig. 7. The components of the extrusion die set (container, ram, mandrels, bolster and die cavity).

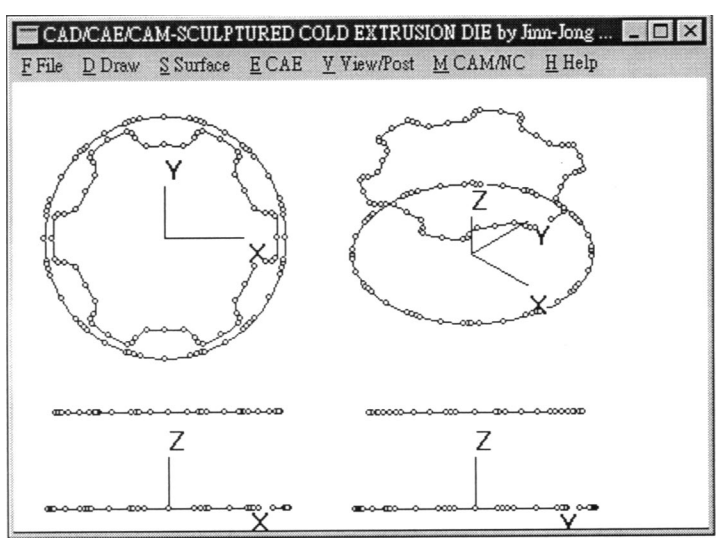

Fig. 8. The product and the billet profiles and the fitting points of a gear spline.

at the transition areas in finishing operation. After the filter of interference, the cutter locations without gauging are shown in Fig. 11(b). The NC codes are sent to the three-axis CNC machine center by using a RS 232 interface to cut the EDM electrodes. Fig. 12 shows the finish cutting operation. After machining, the electrodes are polished in order to obtain a finer surface quality.

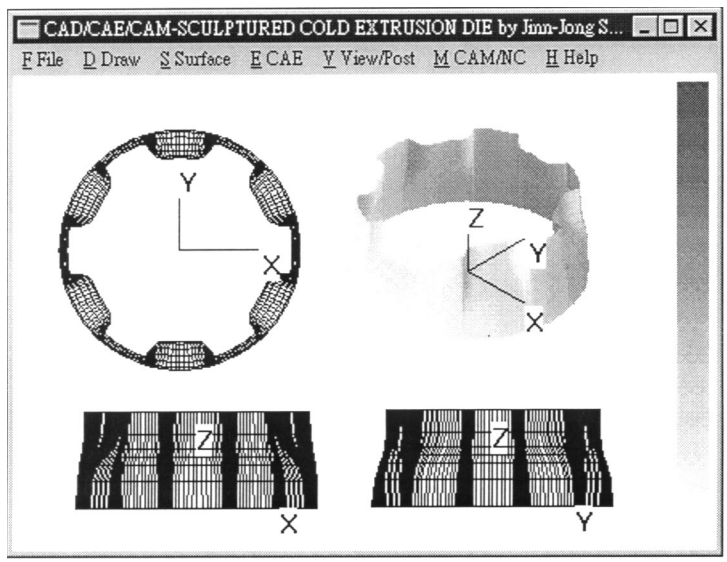

Fig. 9. The optimum die surface for the hollow extrusion of gear spline.

The inner walls of the die cavity are polished and are heat treated to obtain a smooth and hard die surface.

7.3. Extrusion experiments

The solid and the hollow billets are used for the extrusion tests. In Fig. 13, the upper half shows the billets and the lower half shows the extrusion results. The products are straight without bending or twisting. It means the material flows have been controlled smoothly by using the proposed surface die. The comparison of the theoretical pressures and the experimental results with respect to the different area reduction ratio is shown in Fig. 14. The theoretical tendency of the extrusion pressure with respect to the area reduction ratio is in good agreement with the experimental results. The theoretical curve is higher than the experimental curve because the upper-bound method is adopted.

7.4. Applications of die surface design for a fin-tube extrusion

A die surface for the fin-tube extrusion is given to demonstrate the application of the proposed system. The relations of the extrusion pressure, the effective strain and the reduction of area with respect to the relative tooth height is shown in Fig. 15. The tendency of the extrusion pressure and the effective strain is going down with increasing the relative tooth height until the relative tooth height achieved 0.2. The tendency of extrusion pressure and effective strain is then going up with increasing the relative tooth height. It shows that the reduction of area dominates the deformation in the case of low relative tooth height, i.e. higher area reduction requires higher extrusion pressure. The effective strain is increased after the relative tooth height is larger than 0.2 and the tendency of extrusion pressure is going up too. It means the non-uniform flow near

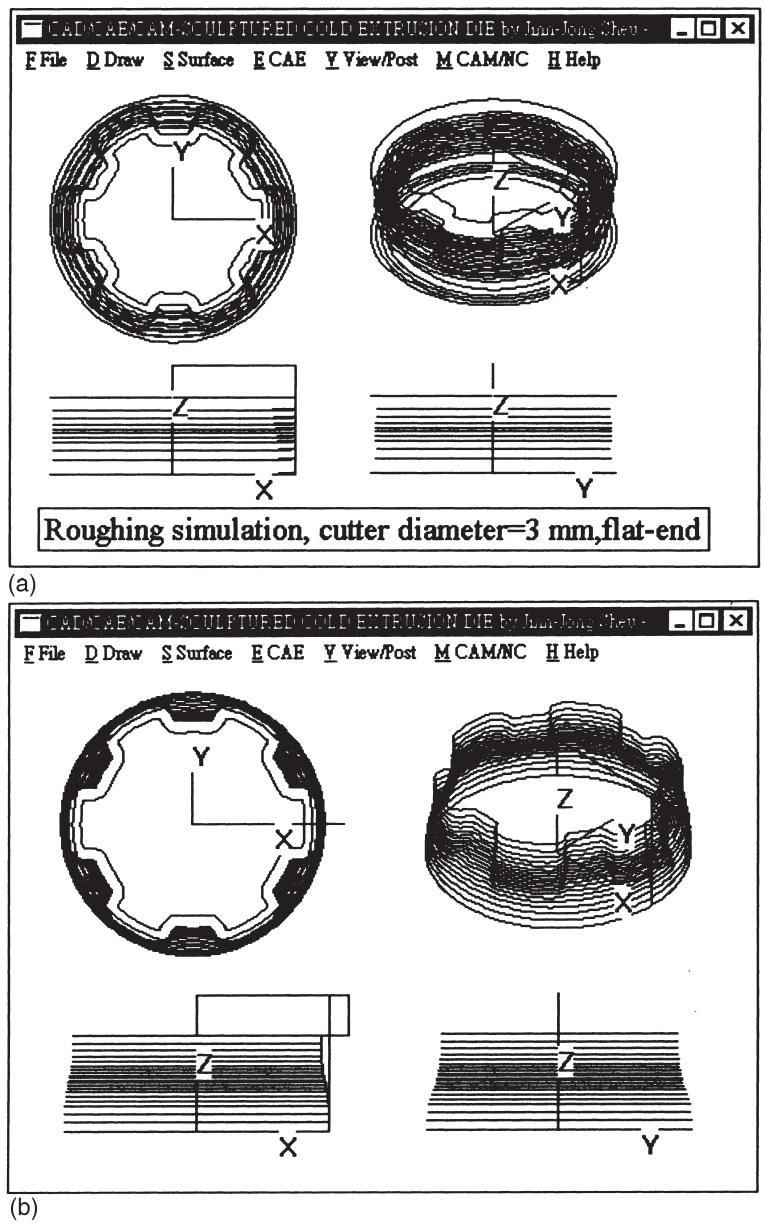

Fig. 10. (a) The tool path simulation of rough cutting for the electrode manufacturing. (b) The tool path simulation of finish cutting for the electrode manufacturing.

the teeth dominates the deformation of material. The deformed grids and the velocity field on the section of zero degrees are shown in Fig. 16(a,b). The deformed grids and the velocity field on the section of 45 degrees are shown in Fig. 16(c,d). These figures show the material flows near the tooth top are not so smooth as the material flows near the circular areas. A non-uniform axial

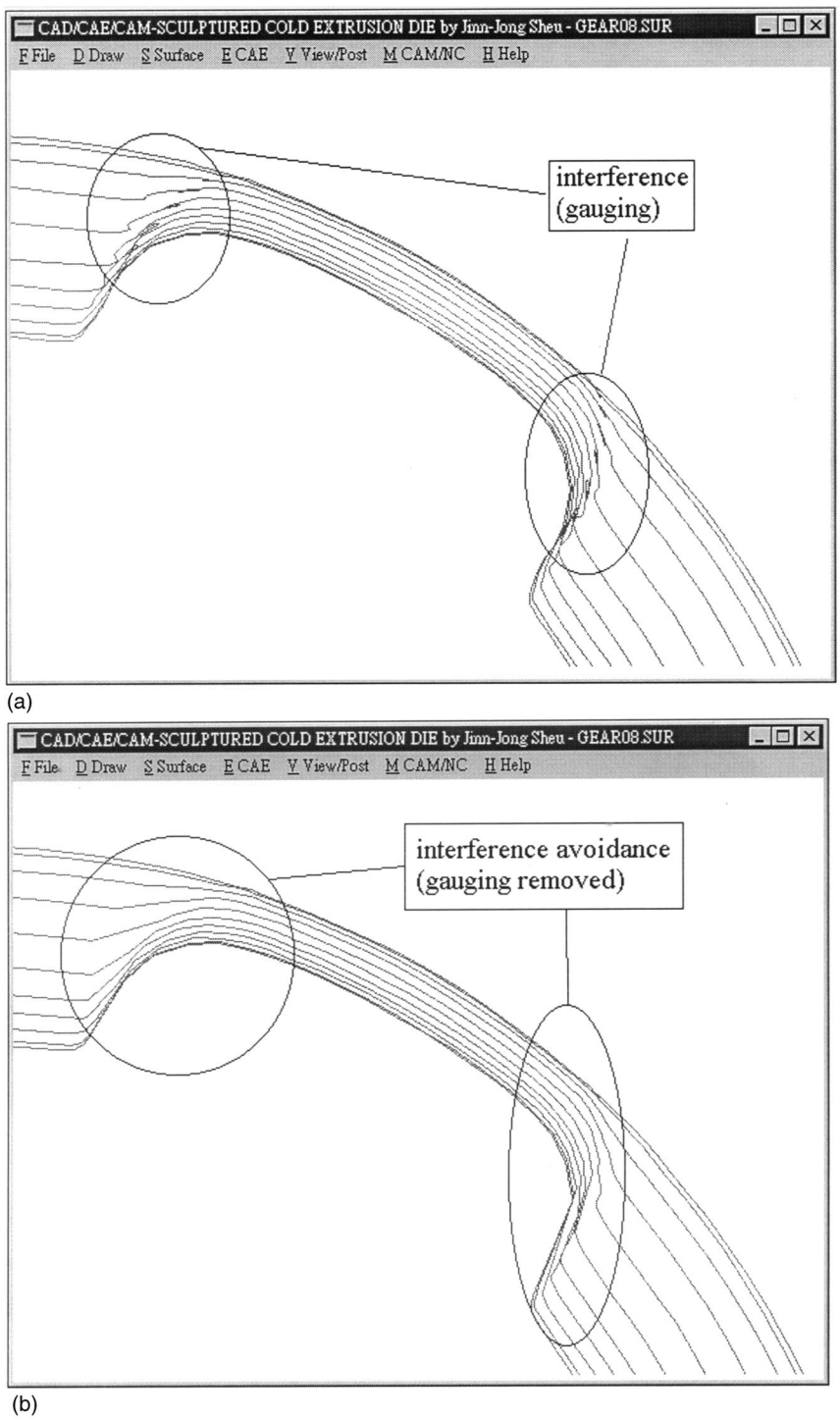

Fig. 11. (a) The finish tool path without interference removal (gauging occurs). (b) The finish tool path with interference removal (no gauging occurs).

Fig. 12. The finish cutting of the electrode of EDM (with ball-end cutter).

velocity is observed because there are friction effects at the areas of die-material and the mandrel-material interfaces.

8. Conclusions

An CAD/CAE/CAM integration system for the design and manufacturing of a sculpture surface for cold extrusion die has been developed. The proposed sculpture surface with the variable control points is able to design the die surface of hollow cold extrusion automatically. The sculpture die surface is optimized to give a lower power consumption by using the upper-bound method and the optimization techniques. The cutter locations are calculated and the interference areas of the tool path are removed. The EDM electrodes are cut successfully to verify the NC codes generated by the proposed system is applicable to the three-dimensional cutting of surface. The tendency of the theoretical results are in good agreement with the extrusion experiments. A die surface design of the fin-tube extrusion is given to demonstrate the application of the proposed system.

Acknowledgements

The author would like to thank the financial support of the National Science Council, the project number is NSC85-2212-E-269-001.

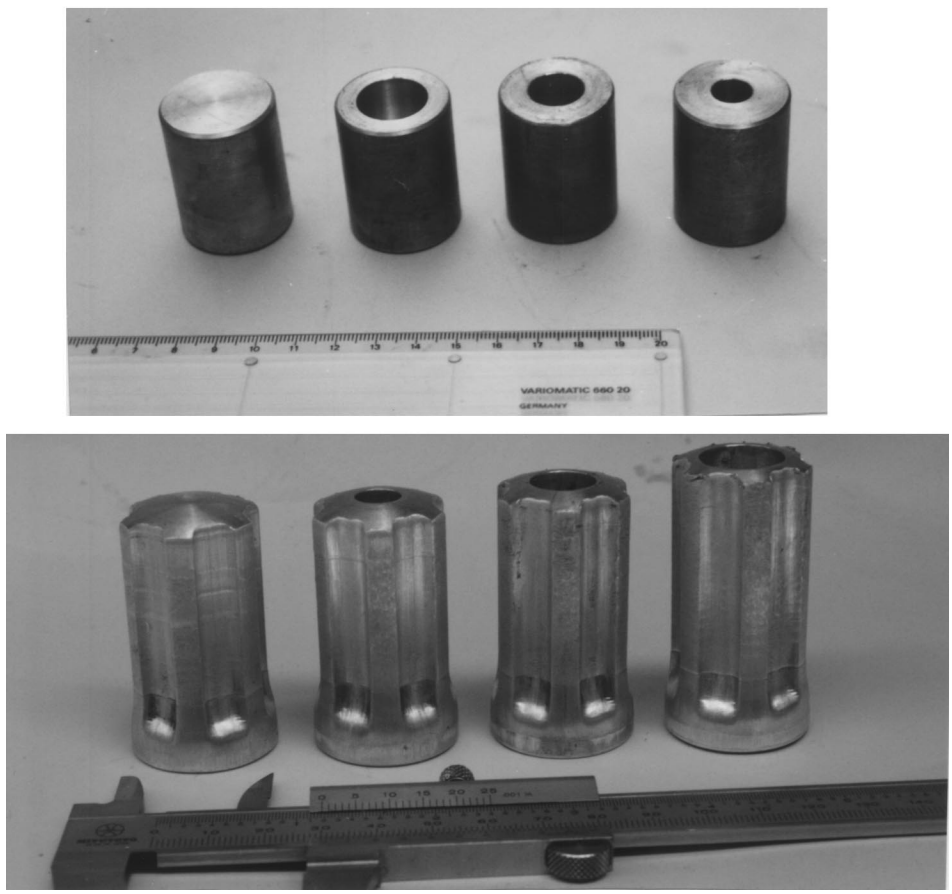

Fig. 13. The hollow billets and the extruded products with different inner radius.

References

[1] M. Kiuchi, H. Kishi, M. Ishikawa, J. of Japan Society Tech. Plasticity 24 (266) (1983) 290.
[2] M. Kiuchi, M. Ishikawa, J. of JSTP 24 (270) (1983) 722.
[3] M. Kiuchi, Proceeding of 12th North American Metalworking Research, 1984, p. 111.
[4] M. Kiuchi, S. I-i-jima, Advanced Technology of Plasticity, vol. 1, 1987, p. 507.
[5] V. Nagpal, C.H. Billhardt, T. Altan, J. of Engng. Ind. ASME 101 (1979) 319.
[6] S. Hoshino, J.S. Gunasekera, Proceeding of the 21st Int. Machine Tool Design and Res. Conf., Swansea, England, 1980, p. 97.
[7] J.S. Gunasekera, S. Hoshino, J. of Eng. for Ind., ASME 107 (Aug. 1985) 229.
[8] D.Y. Yang, K. Lange, Int. J. Mech. Sci. 26 (1984) 1.
[9] D.Y. Yang, C.H. Han, M.U. Kim, Int. J. Mech. Sci. 28 (8) (1986) 517.
[10] C.H. Han, D.Y. Yang, M. Kiuchi, Int. J. Mech. Sci. 28 (4) (1986) 201.
[11] C.H. Han, D.Y. Yang, Int. J. Mech. Sci. 30 (1) (1988) 13.
[12] D.Y. Yang, H.S. Kim, C.M. Lee, C.H. Han, Int. J. Mech. Sci. 32 (2) (1990) 115.
[13] J.J. Sheu, R.S. Lee, Int. J. Mach. Tools Manufact. 31 (4) (1991) 521.
[14] I.D. Faux, M.J. Pratt, Computational Geometry for Design and Manufacture, Halsted Press, New York, Ellis Horwood, 1979, p. 198.

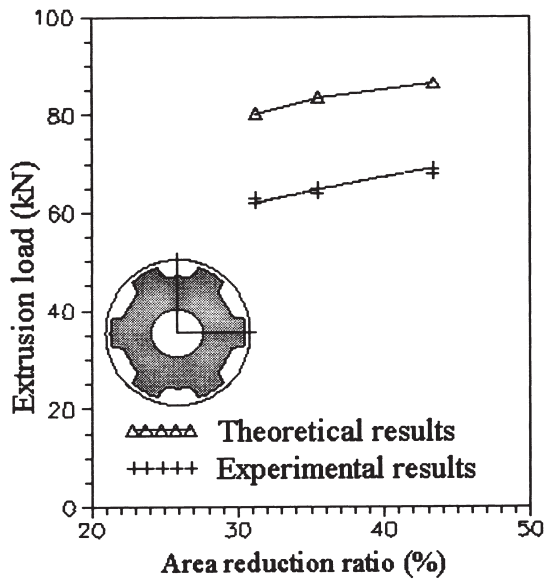

Fig. 14. The comparison of the theoretical extrusion load with the theoretical results.

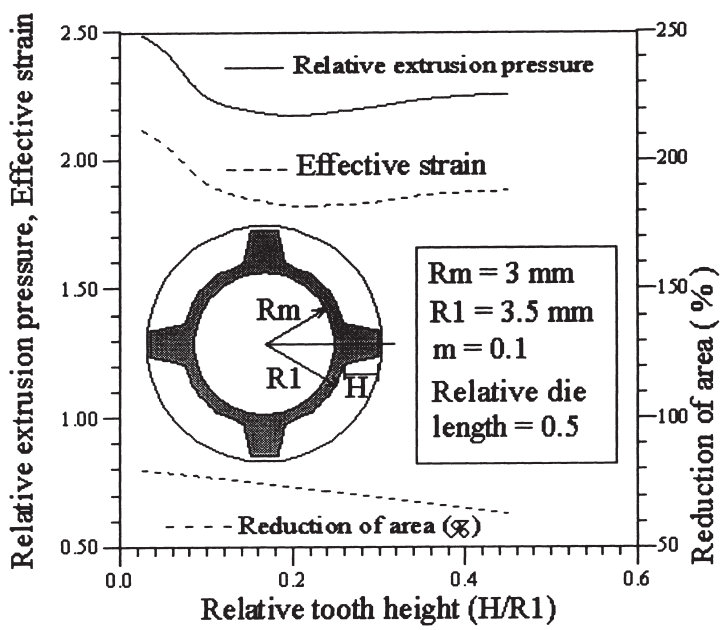

Fig. 15. The relative extrusion pressure and effective strain with respect to the relative tooth height.

[15] P. Broomhead, M. Edkins, Int. J. Prod. Res. 24 (1) (1986) 11.
[16] G.C. Loney, T.M. Ozsoy, Computer-Aided Design, 19 (2) (1987) 85.
[17] B.K. Choi, C.S. Jun, Computer-Aided Design, 21(6) (1989) 371.
[18] G.N. Vanderplaats, Numerical Optimization Techniques for Engineering Design: with Application, McGraw-Hill, New York, 1984, p. 92.

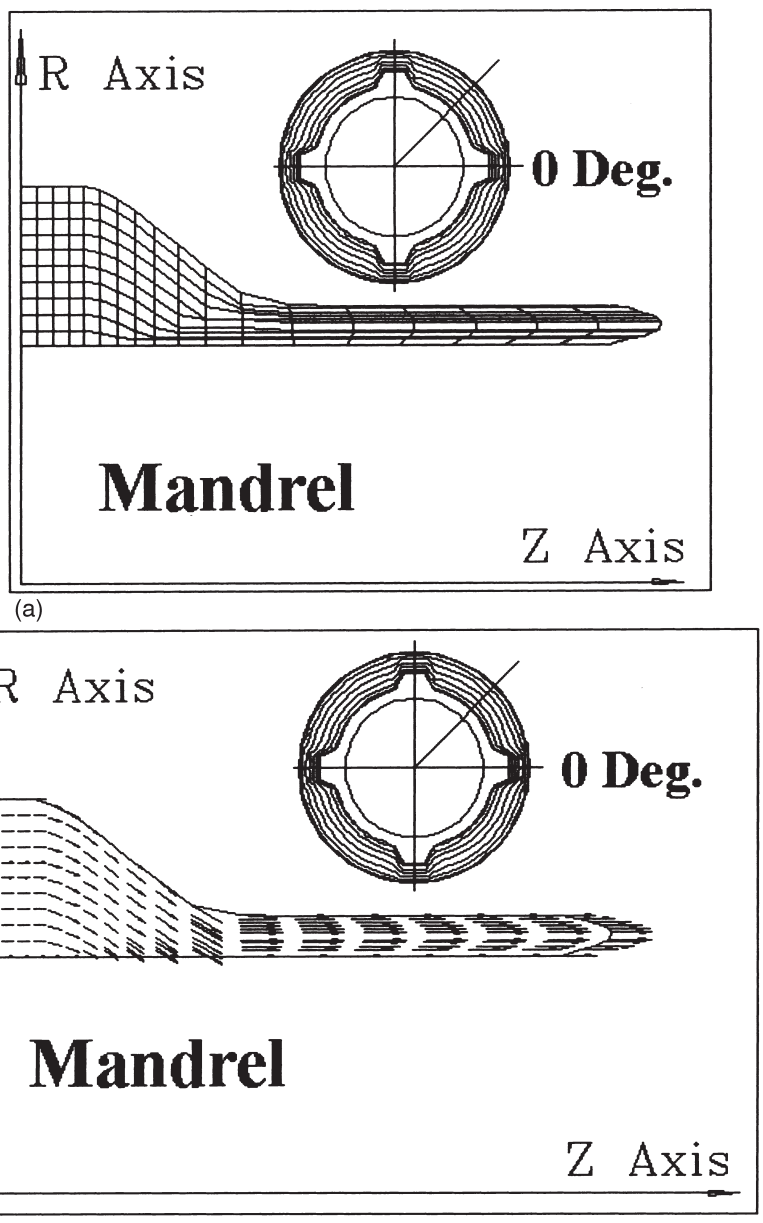

Fig. 16. (a) The deformed grids on the section of 0°. ($H/R1 = 0.2$, $R_m = 3$ mm). (b) The velocity field on the section of 0°. ($H/R1 = 0.2$, $R_m = 3$ mm). (c) The deformed grids on the section of 45°. ($H/R1 = 0.2$, $R_m = 3$ mm). (d) The velocity field on the section of 45°. ($H/R1 = 0.2$, $R_m = 3$ m).

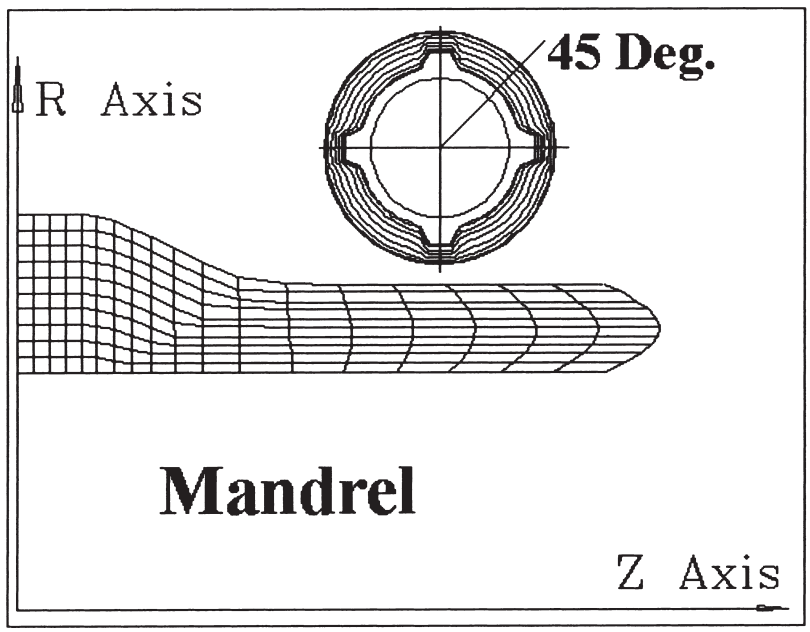

(c)

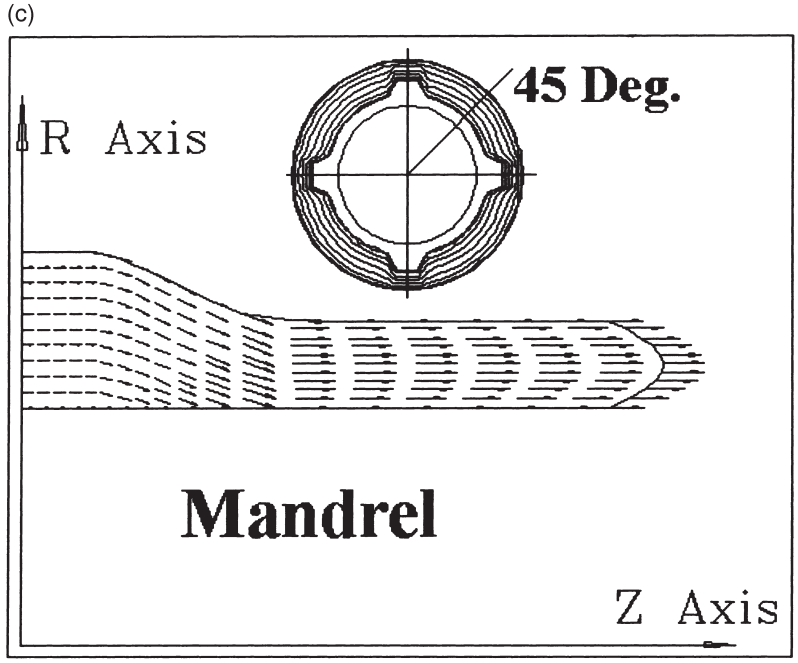

(d)

Fig. 16. Continued.